Swansea University
Prifysgol Abertawe

Cronfa
Setting Research Free

Cronfa - Swansea University Open Access Repository

This is an author produced version of a paper published in:
Inorganic Chemistry

Cronfa URL for this paper:
http://cronfa.swan.ac.uk/Record/cronfa51905

Paper:
Stanulis, A., Katelnikovas, A., Salak, A., Seibutas, P., Ivanov, M., Grigalaitis, R., Banys, J., Kareiva, A., Ramanauskas, R. et. al. (2019). Temperature-Induced Structural Transformations in Undoped and Eu3+-Doped Ruddlesden–Popper Phases Sr2SnO4 and Sr3Sn2O7: Relation to the Impedance and Luminescence Behaviors. *Inorganic Chemistry, 58*(17), 11410-11419.
http://dx.doi.org/10.1021/acs.inorgchem.9b00958

This item is brought to you by Swansea University. Any person downloading material is agreeing to abide by the terms of the repository licence. Copies of full text items may be used or reproduced in any format or medium, without prior permission for personal research or study, educational or non-commercial purposes only. The copyright for any work remains with the original author unless otherwise specified. The full-text must not be sold in any format or medium without the formal permission of the copyright holder.

Permission for multiple reproductions should be obtained from the original author.

Authors are personally responsible for adhering to copyright and publisher restrictions when uploading content to the repository.

http://www.swansea.ac.uk/library/researchsupport/ris-support/

Temperature-induced structural transformations in undoped and Eu^{3+}-doped Ruddlesden-Popper phases Sr_2SnO_4 and $Sr_3Sn_2O_7$: relation to the impedance and luminescence behaviors

Andrius Stanulis[a,b*], Arturas Katelnikovas[c], Andrei N. Salak[d], Povilas Seibutas[e], Maksim Ivanov[e], Robertas Grigalaitis[e], Juras Banys[e], Aivaras Kareiva[f], Rimantas Ramanauskas[b], and Andrew R. Barron[a,g,h*]

[a]*Energy Safety Research Institute (ESRI), Swansea University, Bay Campus, Swansea, SA1 8EN, UK*
[b]*Department of Electrochemical Materials Science, Center for Physical Sciences and Technology, Sauletekio Av. 3, Vilnius, LT−10257, Lithuania*
[c]*Department of Analytical and Environmental Chemistry, Faculty of Chemistry and Geosciences, Vilnius University, Naugarduko 24, Vilnius, LT−03225, Lithuania*
[d]*Department of Materials and Ceramics Engineering, CICECO – Aveiro Institute of Materials, University of Aveiro, Aveiro, 3810−193, Portugal*
[e]*Institute of Applied Electrodynamics and Telecommunications, Faculty of Physics, Vilnius University, Sauletekio Av. 9, III Bld, Vilnius, LT−10222, Lithuania*
[f]*Department of Inorganic Chemistry, Faculty of Chemistry and Geosciences, Vilnius University, Naugarduko 24, Vilnius, LT−03225, Lithuania*
[g]*Department of Chemistry, Rice University, Houston, Texas 77005, USA*
[h]*Department of Materials Science and Nanoengineering, Rice University, Houston, Texas 77005, USA*

Abstract: We report that luminescence of Eu^{3+} ion incorporated into Ruddlesden-Popper phases allows monitoring phase transition in powders (instead of single crystals), in a time efficient manner (compared to neutron diffraction), and importantly, with greater sensitivity than previous methods. Crystal structure and dielectric response of undoped and 0.5%Eu^{3+}-doped $Sr_3Sn_2O_7$ ceramics were studied as a function of temperature over the temperature range of 300–800 K. The luminescence studies of 0.5%Eu^{3+}-doped Sr_2SnO_4 and $Sr_3Sn_2O_7$ samples were performed in the temperature range of 80–500 K. These results were compared with the respective dependences for the undoped compounds. The structural transformations in 0.5%Eu^{3+}-doped $Sr_3Sn_2O_7$ were found at 390 and 740 K. The former is associated with the isostructural atomic rearrangement resulted in a negative thermal expansion along two of three orthorhombic crystallographic axes, while the latter corresponds to the structural transition from the orthorhombic *Amam* phase to the tetragonal *I4/mmm* one. A similar temperature behavior with the structural transformations in the same temperature ranges was observed in undoped $Sr_3Sn_2O_7$, although the values of lattice parameters of the Eu^{3+}-doped and undoped compounds were found to be slightly different

indicating an incorporation of europium in the crystal lattice A dielectric anomaly associated with a structural phase transition was observed in $Sr_3Sn_2O_7$ at 390 K. Optical measurements carried out over a wide temperature range demonstrated a clear correlation between structural transformations in Eu^{3+}-doped Sr_2SnO_4 and $Sr_3Sn_2O_7$ and the temperature anomalies of their luminescence spectra; suggesting the efficacy of this method for the determination of subtle phase transformations.

Introduction

Mixed-metal oxides are a class of functional materials that display a wide range of chemical and physical properties, of particular current interest are the ABO_3 perovskites and perovskite-related compounds because they exhibit a vast array of properties, including: ferroelectricity, high T_c superconductivity, colossal magnetoresistance and insulating properties.[1] Despite the variety of these properties, only few perovskites are ferroelectric, or even polar, in their bulk phase. Recent studies have demonstrated how a combination of non-polar structural distortions, associated with a rotation of BO_6 octahedra about one or more of the crystal axes, can induce polarization or ferroelectricity in several families of layered perovskites.[2] By themselves octahedral rotations cannot induce ferroelectricity in simple perovskites, however the combination of octahedral rotations and layered cation ordering can give rise to ferroelectricity in double perovskites, Ruddlesden-Popper (RP), Dion−Jacobson and Aurivillius phases.[2-4]

The Ruddlesden-Popper homologous series of compounds with general formula $(ABO_3)_nAO$ are a well-known family of layered complex oxides, composed of integer number n of ABO_3 perovskite blocks alternated with a single AO rock-salt layer oriented along the crystallographic c-axis.[5-6] In RP phases, A-site can be occupied by alkaline earth and/or rare earth cations and B-site is commonly occupied by a transition metal with 2+ or 4+ valence (Sn^{4+}, Ti^{4+}, Ni^{2+}, Mn^{4+}, Mn^{2+}, Ru^{4+}). Recently, the hybrid improper ferroelectric mechanism theoretically predicted by Benedek and Fennie[7] in ordered perovskites and the Ruddlesden-Popper compounds ($Ca_3Ti_2O_7$, $Ca_3Mn_2O_7$ and $(Ca/Sr/Ba)_3(Sn/Zr/Ge)_2O_7$) has been experimentally confirmed in the bulk single crystals of $(Ca,Sr)_3Ti_2O_7$ and $Sr_3Sn_2O_7$.[8-9]

Low temperature (12–295 K) high-resolution neutron powder diffraction studies of $Sr_{n+1}Sn_nO_{3n+1}$ (n = 1 and n = 2) were first reported by Green *et al.*,[10-11] and extension of the analysis range towards higher temperature region (12–873 K) showed a rich structural phase diagram for Sr_2SnO_4.[12-13] However, there is a lack of structural information for $Sr_3Sn_2O_7$ at higher temperatures. Therefore, the original objective of

the present work was to study the crystal structure and dielectric behavior of $Sr_3Sn_2O_7$ above room temperature.

Recent studies have demonstrated that incorporation of Sm^{3+} and Eu^{3+} into the $Sr_3Sn_2O_7$ crystal lattice results in luminescence, mechanoluminescence and photochromism properties.[14-17] It is well known, that lanthanides introduced into perovskite type structure are very sensitive to the changes in the coordination environment. Among all the Ln^{3+} ions, Eu^{3+} ion is considered to be the most useful spectroscopic probe due to its non-degenerate emissive state of $^5D_0$ and the ground state $^7F_0$.[18] The trivalent europium ion is often used as a probe for estimation of site symmetry of metal ion, to evaluate crystal field strength and to assess crystal defects in the solid state.[19-20] In our previous work, we showed that temperature dependent lifetime measurements can be successfully applied to monitor phase transitions in Pr^{3+}-doped $SrSnO_3$ ($n = \infty$).[21]

Discontinuous changes in optical parameters occur during temperature changes through phase transitions of insulating materials. Luminescence routes to detect phase transitions are powerful tools but have a tiny literature and so the subject is ideal for rapid exploitation and development.[22] Therefore, the second aim of this work, was to synthesize Eu^{3+} activated $Sr_{n+1}Sn_nO_{3n+1}$ ($n = 1$ and $n = 2$) phosphors by sol-gel method and compare the temperature dependent lifetime measurement results with structural and electrical data.

Experimental

Materials. Strontium carbonate ($SrCO_3$, Aldrich, ≥99.9%) and tin(IV) oxide (SnO_2, Merck, ≥99%) were used in solid state reaction. Tin(II) oxalate (SnC_2O_4, Alfa Aesar, 98%), hydrogen peroxide (H_2O_2, Acros Organics, 35 wt% in H_2O, for analysis, stabilized), citric acid ($C_6H_8O_7$, Sigma-Aldrich, ≥99,5%), strontium hydroxide octahydrate ($Sr(OH)_2{\cdot}8H_2O$, Alfa Aesar, 99%), europium(III) oxide (Eu_2O_3, Sigma-Aldrich, 99.99%) and ammonia (NH_3, Merck, 32% in H_2O, extra pure) were used as starting materials in sol-gel synthesis.

Solid state synthesis. The stoichiometric amounts of raw materials ($SrCO_3$, SnO_2) were thoroughly mixed in the agate mortar using acetone as grinding media. The obtained mixture was dried, transferred to the alumina crucibles and annealed at 1400 °C for 10 h (5 °C/min). After intermediate grinding, the powders were pelletized and sintered at 1500 °C for 10 h in air.

Sol-gel synthesis. The undoped and Eu^{3+}-doped Sr_2SnO_4 and $Sr_3Sn_2O_7$ samples were synthesized by a modification of a previously reported aqueous sol-gel method.[23] The Eu(III) citrate precursor was prepared by dissolving Eu_2O_3 in a 3 M citric acid solution constantly stirring at 80 °C until solution became clear. The pH of all precursors was adjusted to ~7 using ammonia solution, and the total metal ion to citric acid ratio was 1:6. For the preparation of undoped host materials the Sr(II) citrate precursor and citrato peroxo Sn(IV) precursor were mixed in the stoichiometric ratios 2:1 and 3:2 resulting in powders with nominal chemical composition of Sr_2SnO_4 and $Sr_3Sn_2O_7$, respectively. Two series of samples with the Eu^{3+} content ranging from 0.1 to 16 mol-% in Sr_2SnO_4 and $Sr_3Sn_2O_7$ were produced. Stoichiometric mixtures of Sr(II) citrate, Eu(III) citrate and citrato peroxo Sn(IV) precursors corresponding to the compositions $(Sr_{1-x}Eu_x)_2SnO_4$ and $(Sr_{1-x}Eu_x)_3Sn_2O_7$ were prepared. The bi- and tri-metallic precursors were homogenized constantly stirring at 80 °C for 1 h. The dehydration was promoted by increasing temperature sup to ~100 °C, which led to the formation of white foams gradually turning into brown-black gels. The highly hydroscopic Sr(Eu)-Sn gels were dried in the oven at 150 °C for 2 days. Dried gels were ground in an agate mortar and preheated at 500 °C for 5 h with a heating rate of 1 °C/min in air. After an intermediate grinding the samples were additionally sintered at higher temperatures to obtain the desired phase.

Characterization methods

The preliminary studies of phase content were performed using Rigaku MiniFlex II diffractometer working in the Bragg–Brentano (θ/2θ) focusing geometry. The data were collected within 2θ angle from 10° to 80° at a step of 0.02° and integration time of 1 s using Ni-filtered Cu-K_α line. The detailed X-ray diffraction study of the powders was performed using a PANalytical X'Pert MPD PRO diffractometer (Ni-filtered Cu-K_α radiation, PIXcel^{1D} detector, and an exposition corresponding to about 2 s per step of 0.02° over the angular range of 15–95°) at room temperature. In-situ XRD measurements were conducted in an Anton Paar HTK 16N high-temperature chamber in a temperature range between 300 and 900 K. A dwell time before the XRD data collecting at each temperature point was 1 min. Rietveld refinement of the crystal structure was performed using the FullProf program.[24] In order to meet the requirement of electroneutrality of the 0.5%Eu^{3+}-doped composition, the following distribution of europium over the positions of strontium and tin was used in the structure models considered: 2/5 of Eu^{3+} in Sr^{2+} positions, 3/5 of Eu^{3+} in Sn^{4+} positions. Regarding the former, it was suggested that europium is distributed proportionally to the occupations of strontium in positions Sr1 and Sr2 in $Sr_3Sn_2O_7$ structure. The

morphology of synthesized powders and final ceramics was characterized by scanning electron microscopy (SEM) performed with a Hitachi SU-70 field-emission scanning electron microscope (FE-SEM), see Figure S5-S7 in Supporting Information. The thermal decomposition of Sr-Sn-O gel was analyzed through thermogravimetric and differential scanning calorimetry (TG-DSC) analysis using Perkin Elmer STA 6000 Simultaneous Thermal Analyzer (see Figure S2 in Supporting Information). Dried gel sample of about 6 mg was heated from 25 to 950 °C at a heating rate of 10 °C/min in a dry air flow (20 mL/min). The density of the ceramics was found using Archimedes' method by weighting the sample in air and water. The obtained value of density of the $Sr_3Sn_2O_7$ ceramics was 5.3 ± 0.2 g/cm^3, which corresponds to 88 % of theoretical density (6.03 g/cm^3) of the material.[25] The dielectric measurements were performed in 100 Hz–1 MHz frequency range using HP 4284A precision LCR meter. The sample had silver contacts. The measurements were performed in 100–1000 K temperature range during cooling cycle with a temperature variation rate of 1 K/min. Excitation (excitation bandwidth 0.5 nm and emission bandwidth 1.5 nm) and emission (excitation bandwidth 5.0 nm and emission bandwidth 0.5 nm) spectra were recorded in the ranges 250–550 and 500–800 nm, respectively, on an Edinburgh Instruments FLS980 fluorescence spectrometer equipped with a 450W Xe arc lamp, mirror optics for powder samples and a Peltier cooled (-20 °C) single-photon counting photomultiplier (Hamamatsu R2658P). The photoluminescence emission spectra were corrected using a calibrated tungsten incandescent lamp certified by the NPL (National Physics Laboratory, UK) and excitation spectra were corrected with a reference detector. Decay curves were recorded with an Edinburgh Instruments FLS980 spectrometer quipped with an Edinburgh Instruments mF900 flash lamp and a Hamamatsu extended red sensitivity photomultiplier tube. Data was acquired in a gated single photon counting (MCS) mode. The decay time fitted into a single exponential function did not converge and resulted in high Chi-square values. Temperature dependent decay time values of Sr_2SnO_4:0.5%Eu^{3+} and $Sr_3Sn_2O_7$:0.5%Eu^{3+} fitted using mono-exponential decay function are presented in Figure S12-S14. All measurements were performed at room temperature in air. For thermal quenching (TQ) measurements a cryostat ‘‘MicrostatN’’ from Oxford Instruments has been applied to the present spectrometer. Liquid nitrogen was used as a cooling agent. Measurements were carried out from 80 to 500 K in 20 K steps.

Results and discussion

The phase formation and purity of undoped and Eu^{3+}-doped Sr_2SnO_4 and $Sr_3Sn_2O_7$ samples were monitored by means of XRD analysis (see Supporting Information). It can be summarized that the

formation of these two members of Ruddlesden-Popper compounds are composition dependent. $Sr_3Sn_2O_7$ phase is formed through the intermediate Sr_2SnO_4 phase, which in turn forms through the intermediate $SrSnO_3$ phase. The single phase Eu^{3+}-doped Sr_2SnO_4 and $Sr_3Sn_2O_7$ phosphors were obtained at 1400 and 1500 °C, respectively. Both phosphors are single phase when europium content is up to 0.5 mol-%. Based on these observations, further investigations on the system were carried out on samples, which gave the best output (i.e. Sr_2SnO_4:0.5%Eu^{3+} and $Sr_3Sn_2O_7$:0.5%Eu^{3+}). The Eu^{3+} doping rates in the host materials are rather low. Therefore, one cannot expect any significant changes of the lattice parameters in $Sr_3Sn_2O_7$:0.5%Eu^{3+} nor in Sr_2SnO_4:0.5%Eu^{3+} as compared to the respective undoped compounds.

Besides, it has been revealed from the XRD study of $Sr_3Sn_2O_7$ and Sr_2SnO_4 with different europium doping rates (Figure S4) that the maximum inclusion of Eu^{3+} into host of $Sr_3Sn_2O_7$ and Sr_2SnO_4 is 0.5 % and 4 mol%, respectively is in good agreement with the emission intensity integrals as a function of Eu^{3+} concentration in Figure S8.

Before the in-situ XRD measurements, diffraction data on $Sr_3Sn_2O_7$:0.5%Eu^{3+} were collected at room temperature using a zero-background holder with an exposition of about 6 s per step of 0.01° to resolve the low-intensity reflections. The refinement was performed using either the centrosymmetric orthorhombic structure (space group *Amam*) or the polar orthorhombic structure (*A2$_1$am*).[9, 11] With almost the same goodness of the fit, the essentially similar values of the lattice parameters in both structural models were obtained (Figure 1). The calculated values of the lattice parameters are slightly different from those reported by Green *et al.*[10-11] for undoped $Sr_3Sn_2O_7$ that indicates incorporation of europium into the crystal lattice.

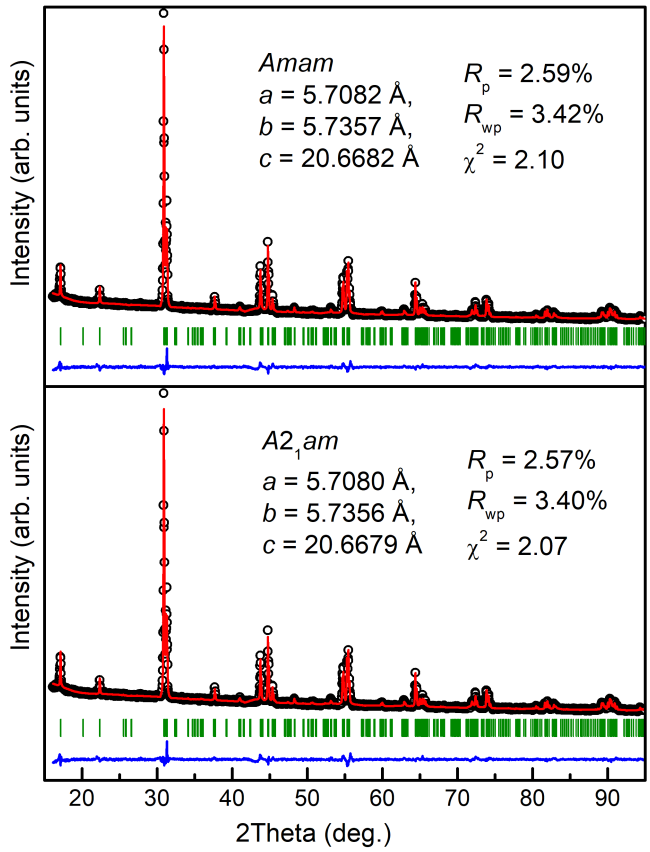

Figure 1. Observed (open circles), calculated (solid line), and difference (below) XRD profiles of $Sr_3Sn_2O_7$:0.5%Eu^{3+} at room temperature refined in space group *Amam* (top panel) and in space group *A2₁am* (bottom panel). Tick marks indicate the positions of Bragg peaks.

Since it was impossible to conclude whether the orthorhombic phase is centrosymmetric or polar, for further consideration of $Sr_3Sn_2O_7$:0.5%Eu^{3+} at room temperature we adopted the *Amam* structure that has been proved from a neutron diffraction study of $Sr_3Sn_2O_7$.[11] It is important to stress here that temperature behavior of lattice parameters of $Sr_3Sn_2O_7$:0.5%Eu^{3+} observed in this work is the same regardless of the model (*Amam* or *A2₁am*) used.

Temperature dependences of the lattice parameters of $Sr_3Sn_2O_7$:0.5%Eu^{3+} are shown in Figure 2. A near linear increase of the parameters with temperature is observed until about 400 K. In the temperature range of about 410–430 K, both *a* and *b* decreases, while *c* increases. It should be pointed out that in spite of unusual behavior of the lattice parameters in this range (negative thermal expansion along two of three crystallographic axes), no qualitative changes in the XRD patterns, namely appearance/disappearance of reflections or splitting as well as no sign of phase coexistence has been detected. When temperature is increased above 430 K, all the lattice parameters grow again. The *b*-parameter reaches the maximum

value at about 680 K and starts a slow decrease with increasing temperature. Refinement of crystal structure of $Sr_3Sn_2O_7$:0.5%Eu^{3+} at 740 K demonstrated that the data can be equally well fitted either using the orthorhombic *Amam* structure or the tetragonal *I*4/*mmm* one. Difference between values of parameters *a* and *b* in case of the orthorhombic model was below the calculation error. Therefore, $Sr_3Sn_2O_7$:0.5%Eu^{3+} was accepted to be tetragonal above 730 K (Figure 2). For convenience of comparison, the *a*-parameter of the tetragonal phase in Figure 2 is expressed in terms of $\sqrt{2}a$. Above the *Amam* - *I*4/*mmm* phase transition, an increment of *c*-parameter with temperature slows down and after about 780 K the parameter starts decreasing. One should notice that the unit-cell volume grows in a monotonic way both over the range of the phase transition and above, when the *c*-parameter decreases with temperature (Figure 3). Meanwhile, the unit-cell volume increases monotonically.

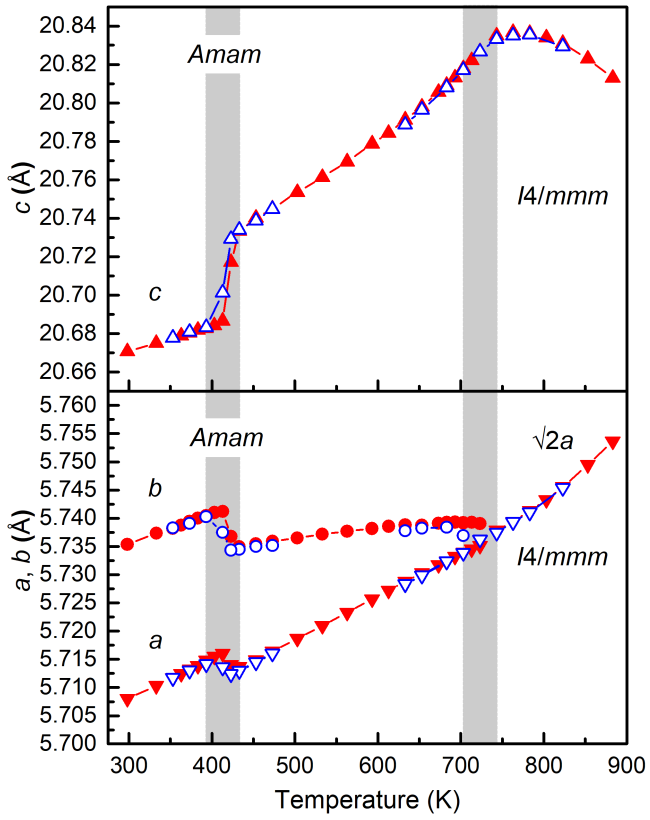

Figure 2. Lattice parameters of $Sr_3Sn_2O_7$:0.5%Eu^{3+} as a function of temperature on heating (red solid symbols) and cooling (blue open symbols). The lines between points are guides to the eye. The range of anomalous temperature behavior of the lattice parameters and the range of the orthorhombic-tetragonal phase transition are indicated.

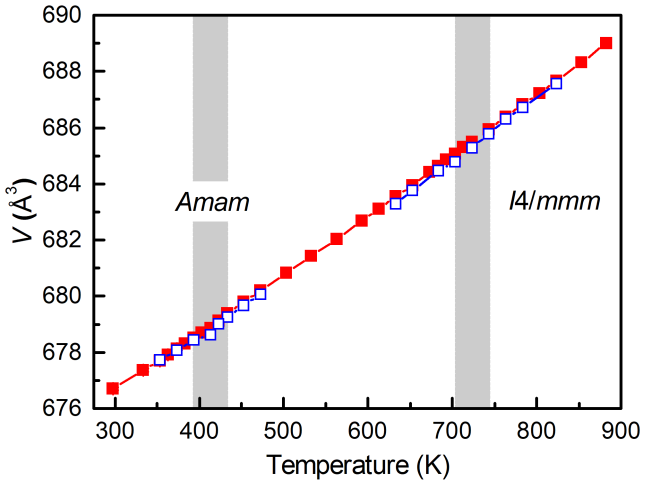

Figure 3. Temperature dependence of the unit-cell volume of $Sr_3Sn_2O_7$:0.5%Eu^{3+} on heating (red solid symbols) and cooling (blue open symbols). For comparison, the doubled values of the unit-cell volume of the tetragonal *I*4/*mmm* phase are plotted for convenience of comparison. The lines between points are guides to the eye.

As seen from Figure 2, the same behavior with a small temperature hysteresis of about 25 K and 10 K (for the higher-temperature range and the lower-temperature range of interest, respectively) is observed upon cooling. We observed the essentially similar temperature dependence of the lattice parameters with the structural transformations in the same temperature ranges in undoped $Sr_3Sn_2O_7$ as well.

Yoshida *et al*. have recently been reported a coexistence of the $A2_1am$ phase and the *Pnab* phase in the range of 390-440 K.[26] Although the temperature phase diagram of $Sr_3Sn_2O_7$ suggested by those authors is richer in terms of the number of phases, the temperature behaviors of the lattice parameters *a*, *b* and *c* in the ranges of orthorhombic phases(s) as well as the behaviors of the parameters *a* and *c* in the range of the tetragonal phase are near the same as those found in this paper. Yoshida *et al*. revealed the negative thermal expansion along the same axes and in the same temperature ranges as those indicated in Figure 2.

We would like to stress here that effect of negative thermal expansion along particular crystallographic axes, which are different in the higher- and the lower-temperature ranges, is observed in $Sr_3Sn_2O_7$:0.5%Eu^{3+} out of the phase transition range. A similar effect was reported for Ruddlesden-Popper perovskite $Ca_3Mn_2O_7$.[27] However, a negative thermal expansion of *c*-parameter in this compound was found in one of two phases in a wide temperature range of the phase coexistence, and a thermal expansion of *c*-parameter in a second phase of $Ca_3Mn_2O_7$ was positive.

Unusual temperature behavior of the lattice parameters in a single phase perovskite $Sr_3Sn_2O_7$:0.5%Eu^{3+} within the same crystal symmetry suggests some relaxation processes. One can assume that the oxygen coordination spheres of Sr^{2+} and/or Sn^{4+} become too distorted with temperature, which results in a redistribution of the bond distances. Similar phenomena have been observed in the monoclinic phase of La_2MgTiO_6 close to room temperature and in the hexagonal high-temperature phase of $YMnO_3$ at about 920 K.[28-29] The latter was classified as an isostructural transition. In both the above-mentioned perovskite compositions, anomalies of dielectric behavior were observed in the respective temperature ranges.

The real and imaginary parts of complex dielectric permittivity of $Sr_3Sn_2O_7$ ceramics, as a function of temperature, are shown in Figure 4. As seen from the figure, there are three distinct ranges in the temperature dependence of the dielectric permittivity. The material has low relative dielectric permittivity (around 5.1) and low dielectric losses ($\tan \delta < 0.002$) below 390 K. An anomaly in dielectric permittivity is observed at 390 K, which is associated with a structural (most likely, the improper ferroelectric to paraelectric) phase transition. Dielectric losses increase rapidly in the 390–650 K temperature range. The losses are associated with electric conductivity and are accompanied by increase of the real part of dielectric permittivity via charge separation (Maxwell-Wagner relaxation). Influence of the conductivity on the dielectric spectra is inversely proportional to frequency of the measurement, thus permittivity at 1 MHz is affected the least. There are no other anomalies (except for the phase transition at 390 K) observed at this frequency at temperatures below 650 K. The spectra are dominated by conductivity at temperatures above 650 K. However, the losses grow less rapidly as temperature increases, if compared to the 390–650 K range.

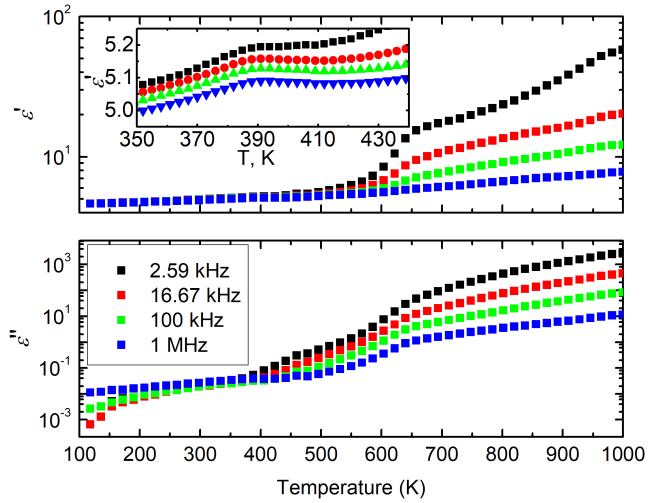

Figure 4. Temperature dependences of the real (top) and imaginary (bottom) parts of complex dielectric permittivity of $Sr_3Sn_2O_7$ ceramics; the inset shows the dependence of the real part in the vicinity of the phase transition.

As the conductivity is highly important at high temperatures, specific impedance was calculated based on the dielectric data. Figure 5 shows frequency dependences of the specific impedance. The points represent experimental data, while solid lines are fits using Eq. 1, where indices 1 and 2 correspond to specific electric resistivity of grains and of the inter-grain medium, respectively; $\Delta\rho$ corresponds to DC specific resistivity, τ is the characteristic mean charge relaxation time, and α is a parameter, which defines distribution of relaxation times. The equation corresponds to two parallel RC circuits (with a constant phase element instead of a capacitor), which are connected in series.

$$\rho^* = \frac{\Delta\rho_1}{(1+j\omega\tau_1)^{\alpha_1}} + \frac{\Delta\rho_2}{(1+j\omega\tau_2)^{\alpha_2}} \quad (1)$$

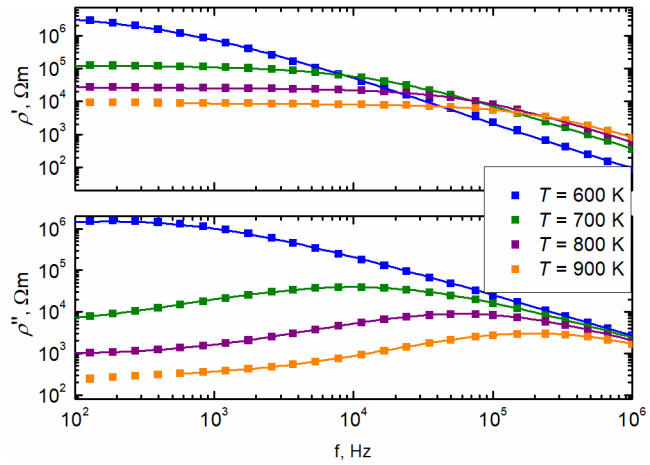

Figure 5. Frequency dependences of the real (top) and imaginary (bottom) parts of complex specific impedance of $Sr_3Sn_2O_7$ ceramics.

There is enough data in the spectra only to get information about one process: charge relaxation inside the grains. Alpha parameter of this process is close to unity (very narrow distribution of relaxation times). This is most likely due to absence of dielectric dispersion in the grain medium. The other parameters: DC specific resistivity and charge relaxation time inside grains, are presented in Figure 6 versus reciprocal temperature. The solid straight lines correspond to Arrhenius equation (Eq. 2), where x corresponds to either $\Delta\rho$ or τ, and x_0 is the value of the parameter at an infinite temperature, E_a is activation energy, and k is the Boltzmann constant.

$$x = x_0 e^{-\frac{E_a}{kT}} \qquad (2)$$

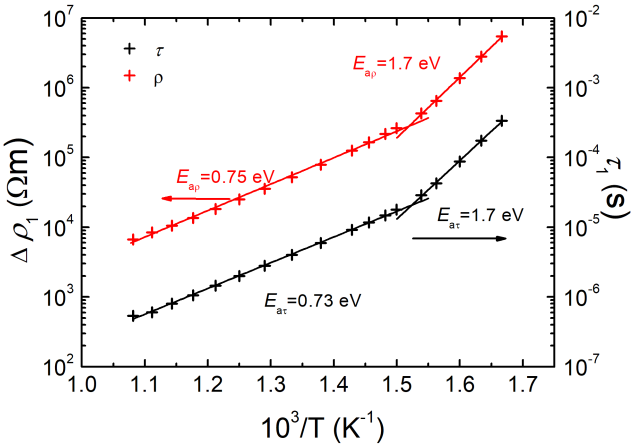

Figure 6. Reciprocal temperature dependence of DC resistivity (red) and charge relaxation times (black) of the grains of $Sr_3Sn_2O_7$ ceramics.

As can be seen from Figure 6, charge relaxation time has the same activation energy as specific DC resistivity at a selected temperature. This means, that dielectric permittivity has very slight or no variation at temperatures higher than 650 K. Below 650 K, the activation energy is rather high, namely 1.7 eV. The bandgap of $Sr_3Sn_2O_7$ is around 4 eV.[17,30] In that case, the activation energy we calculated is close to half the bandgap, but too small to imply conductivity through intrinsic electrons. Very deep (donor or acceptor) defects must be present in the material, thus contributing to the total electrical conductivity. There is a decrease in activation energy at 650 K to 0.73–0.75 eV value. Such a change is possible if the main electrons/holes responsible for conductivity are originating from ionized dopants. This means that all deep defects are ionized at 650 K, and increase in conductivity at higher temperatures is due to increasing mobility of the charge carriers. Another, much less likely possibility, is that the main charge carriers are intrinsic electrons, and the change in activation energy implies a change of bandgap from 3.4 to 1.5 eV at 650 K. However, this option is not well supported by the current data, as the XRD investigations show a phase transition above 700 K, and there is no anomaly observed in either the dielectric or electrical properties. Furthermore, the band gap of 3.4 eV is too small in comparison to what is presented in the literature.

On a side note, an attempt to electrically switch the polarization of the ceramics was made. Unfortunately, no switching was observed even in 100 kV/cm fields at room temperature. The switching energy of $Sr_3Sn_2O_7$ is equal to 37 meV,[3] and is comparable to classical proper ferroelectrics (i.e., 20 meV for $BaTiO_3$[31] and 30 meV for $PbTiO_3$[32]). This means that either the actual switching energy in our case is much higher due to defects, or the material could be pyroelectric. The first case is quite possible, as deep signatures of deep defects are observed in the impedance data. Hardening can be observed, if the donors are acceptors.[33] The second case (pyroelectric origin) would contradict the theoretical calculations and experimental results.[9] However, it is possible that the coercive field in the ceramics is higher than predicted for single crystals due to additional mechanical stresses, which are always present in any ceramics.

Figure 7 shows the excitation and emission spectra of Sr_2SnO_4:0.5%Eu^{3+} and $Sr_3Sn_2O_7$:0.5%Eu^{3+} samples at room temperature. The excitation spectrum of Sr_2SnO_4:0.5%Eu^{3+} and $Sr_3Sn_2O_7$:0.5%Eu^{3+} phosphors are very similar and show a broad absorption band at 300 nm, which corresponds to the transition from the $^7F_0$ ground state to the charge transfer (CT) state due to oxygen to europium

interaction. The electrons move from completely filled 2p orbitals of O^{2-} to partially filled $4f^6$ levels of Eu^{3+}.[34] Several groups of sharp lines ranging from 350 to 550 nm are assigned to typical f-f transitions of trivalent europium ion. The emission spectra of Sr_2SnO_4:0.5%Eu^{3+} and $Sr_3Sn_2O_7$:0.5%Eu^{3+} excited with different wavelengths are shown in Figure 7a and Figure 7b, respectively. The luminescence spectra of both phosphors are consistent with low symmetry environment around Eu^{3+} ion.

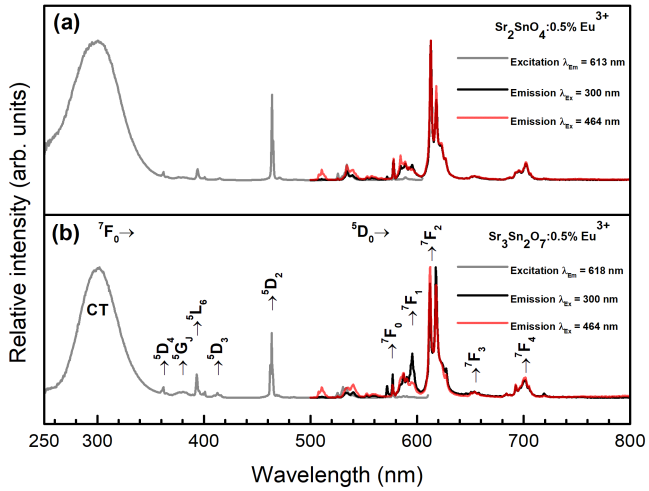

Figure 7. Photoluminescence excitation and emission spectra of (a) Sr_2SnO_4:0.5%Eu^{3+} and (b) $Sr_3Sn_2O_7$:0.5%Eu^{3+} phosphors at room temperature.

The numbers of observed $^5D_0 \rightarrow {}^7F_J$ emission lines correspond to intra-4f-shell transitions from the excited level $^5D_0$ to lower levels ^7F_J (J = 0, 1, 2, 3, 4) for Eu^{3+} ions and can be used to distinguish Eu^{3+} in different symmetry sites. The $^5D_0 \rightarrow {}^7F_0$ transition is usually very weak because it is forbidden and can only be observed in hosts with low symmetry (C_s, C_n and C_{nv}). The $^5D_0 \rightarrow {}^7F_0$ transition cannot be split by crystal field, which indicates that every $^5D_0 \rightarrow {}^7F_0$ peak corresponds to a special site.[35-36] Therefore, the observation of the $^5D_0 \rightarrow {}^7F_0$ emission line indicates that Eu^{3+} ions occupy the sites with low symmetry and without an inversion center.

As shown in Figure 7 and Figure 8, the emission spectra of Sr_2SnO_4:0.5%Eu^{3+} and $Sr_3Sn_2O_7$:0.5%Eu^{3+} phosphors also contain emissions from the higher energy levels $^5D_1$ and $^5D_2$. $^5D_{1,2,3} \rightarrow {}^7F_J$ lines usually appear in a compound with low lattice phonon energy, which leads to multiphonon relaxation. They are usually difficult to occur among the levels of Eu^{3+}. The presence of

emission lines from higher excited states of Eu^{3+} is attributed to the low vibration energy of SnO_3^{2-} groups. Multiphonon relaxation by SnO_3^{2-} is not able to bridge the gaps between the higher energy levels and the $^5D_0$ level of Eu^{3+} completely, resulting in weak emissions from these levels. Such emission lines of europium were previously observed in ThO_2 and Sr_2CeO_4 host materials.[20,37] Asymmetric peak shape of $^5D_0 \rightarrow {}^7F_0$ transition in both host materials suggests the presence of two closely similar low symmetry crystallographic sites. The splitting of this transition can be visible in emission spectra of $Sr_3Sn_2O_7$:0.5%Eu^{3+} phosphor (see Figure S9, Supporting Information).

The emission peaks at 589 and 613 nm are due to magnetic dipole allowed $^5D_0 \rightarrow {}^7F_1$ and electric dipole allowed $^5D_0 \rightarrow {}^7F_2$ characteristic transitions of Eu^{3+} ion, respectively (Figure 7). When Eu^{3+} ion occupies a site with inversion symmetry, only magnetic dipole transition is allowed. However, when it occupies a non-centrosymmetric environment, both the electric and magnetic dipole transitions are allowed. The magnetic dipole allowed $^5D_0 \rightarrow {}^7F_1$ transition is insensitive to the chemical environment, whereas electric dipole allowed $^5D_0 \rightarrow {}^7F_2$ transition is hypersensitive to the chemical environment around the Eu^{3+} ion.[38]

Fluorescence measurements in cryogenic conditions improve the spectral resolution of the crystal-field splitting of the ^7F_J transitions, facilitating the spectral analysis. The splitting of $^5D_0 \rightarrow {}^7F_1$ transition by crystal field into seven emission lines can be seen at 80 K in the emission spectra depicted in Figure 8. The number of components of the $^5D_0 \rightarrow {}^7F_1$ transition readily indicates the presence of at least three different Eu^{3+} sites in both host materials.

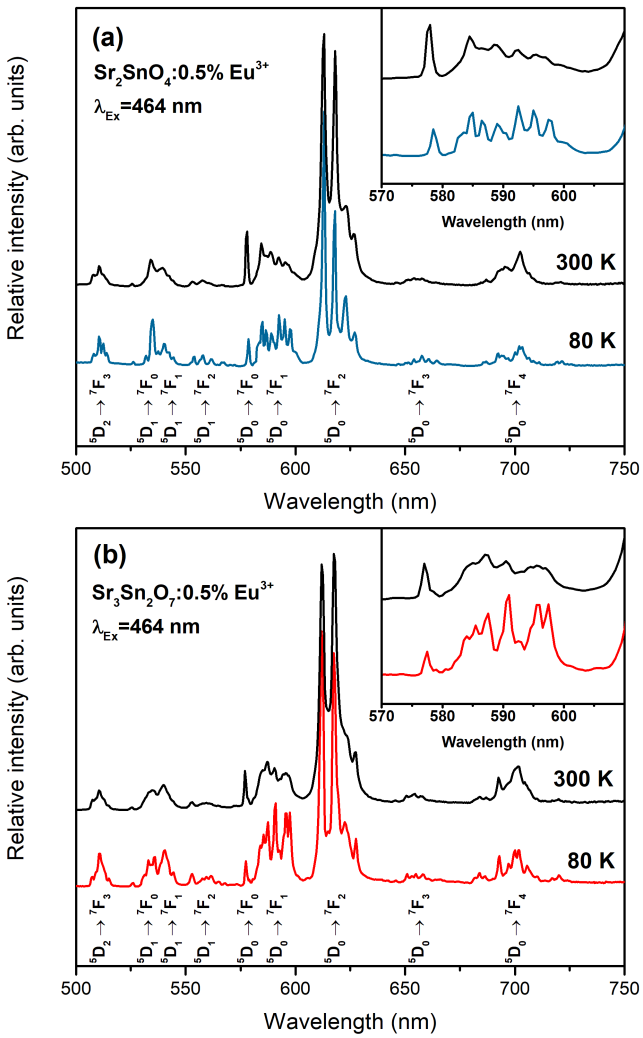

Figure 8. Luminescence emission spectra of (a) Sr_2SnO_4:0.5%Eu^{3+} and (b) $Sr_3Sn_2O_7$:0.5%Eu^{3+} phosphors at 80 and 300 K. The inset represents the magnified $^5D_0 \rightarrow {}^7F_{0,1}$ transitions.

At room temperature, the Sr^{2+} ions in Sr_2SnO_4 are surrounded by nine oxygen ions with seven relatively short and two longer Sr-O bond distances. The coordination polyhedron most closely resembles an idealized tricapped trigonal prism with D_{3h} symmetry. When Sr^{2+} (ionic radii: 1.31 Å) is replaced by a smaller ion, such as Eu^{3+} (ionic radii: 1.12 Å), the SnO_6 octahedron will tilt and two elongated Sr-O bonds become too large to be counted into the coordination sphere of Eu^{3+}/Sr^{2+} ion. Therefore, the coordination number of Eu^{3+}/Sr^{2+} reduces to seven (C_{3v} symmetry). Moreover, the heterovalent substitution of Sr^{2+} by Eu^{3+} creates local strains that lower the symmetry of the site towards C_{2v} due to the charge imbalance around the Eu^{3+}.[12, 39-41]

On the other hand, in nine-coordinated $Nd(BrO_3)_3 \cdot 9H_2O$ and $Ho(BrO_3)_3 \cdot 9H_2O$ complexes the lanthanide ions have approximate D_{3h} symmetry, although the space group determination required only C_{3v} symmetry at the rare-earth-ion site.[42-43] The symmetry of Eu^{3+} ion in nine-coordinated $Eu(BrO_3)_3 \cdot 9H_2O$ complex decreases from D_{3h} to C_{3v} and C_s on cooling, with appearance of several inequivalent ion sites.[44] It is known that C_{2v} symmetry fields cause $^5D_0 \rightarrow {}^7F_1$ and $^5D_0 \rightarrow {}^7F_2$ splitting into 3 and 4 lines, respectively. If Eu^{3+} ions are situated at lower symmetry C_2, C_s or C_1 site, there should be 3 lines for $^5D_0 \rightarrow {}^7F_1$ transition and 5 lines for $^5D_0 \rightarrow {}^7F_2$ transition.[45-47]

Considering that one component of $^5D_0 \rightarrow {}^7F_1$ transition corresponds to Eu^{3+} in centrosymmetric Sn^{4+} site (O_h symmetry), the remaining six components confirm the existence of two closely similar crystallographic sites. As a matter of fact, four and five lines for $^5D_0 \rightarrow {}^7F_2$ transition were resolved in the emission spectra of Sr_2SnO_4:0.5%Eu^{3+} and $Sr_3Sn_2O_7$:0.5%Eu^{3+} at 80 K, respectively (Figure 8). It concludes that the actual site symmetry of Eu^{3+} is very likely reduced to a lower symmetry than C_{2v} due to the difference of ionic radius and charge imbalance between Eu^{3+} and Sr^{2+}. The fact that only 4-5 lines, instead of expected 10, are observed in the $^5D_0 \rightarrow {}^7F_2$ region suggests that the unseen lines are less intense and could be buried under other transitions. To conclude this, the Eu^{3+} ion at Sr^{2+} site does not generate one single emission spectrum, but rather a combination of two very similar spectra (low symmetry C_2, C_s or C_1 site). These latter arise from individual species in which the metal ions experience slightly different crystal-field effects.

In $Sr_3Sn_2O_7$ structure Sr1 is coordinated by twelve nearest oxygen and Sr2 is located at a site nine-coordinated by oxygen.[30] As can be seen in Figure 8b the intensity of $^5D_0 \rightarrow {}^7F_1$ transition in $Sr_3Sn_2O_7$ host is higher than in Sr_2SnO_4. This is due to the increased number of perovskite building blocks in the unit cell and presence of Eu^{3+} in cuboctahedral Sr1 site (more sites with O_h symmetry). Thus, Eu^{3+} ions occupy two different centrosymmetric sites (Sr1 (CN = 12) and Sn (CN = 6)) and two similar sites with C_{2v} or lower symmetry in $Sr_3Sn_2O_7$ host material. For definite identification of observed emission lines relative to the individual sites, the site selective and time resolved photoluminescence spectroscopic studies are required. The emission intensity integrals of Sr_2SnO_4:0.5%Eu^{3+} and $Sr_3Sn_2O_7$:0.5%Eu^{3+} phosphors excited at 464 nm in temperature range of 80–500 K are shown in Figure 9. Evidently, the emission intensity integrals decrease with increasing temperature for both samples.

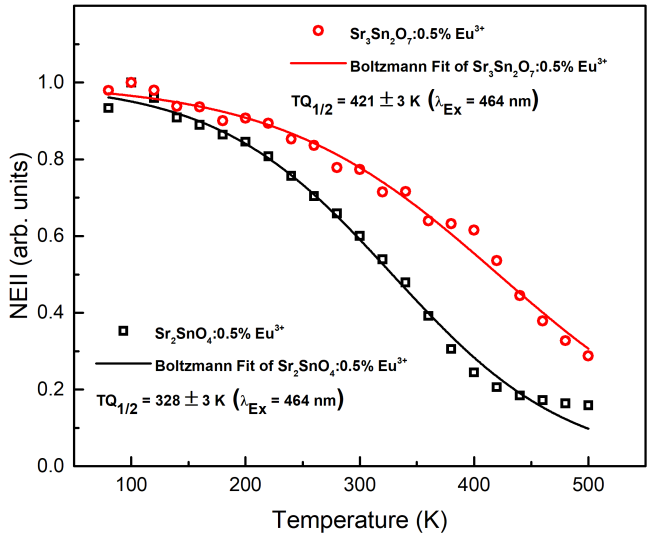

Figure 9. Normalized emission intensity integrals (NEII) of Sr_2SnO_4:0.5%Eu^{3+} and $Sr_3Sn_2O_7$:0.5%Eu^{3+} phosphors as a function of temperature.

For the calculation of $TQ_{1/2}$ values (the temperature, at which phosphor loses half its efficiency) the Boltzmann sigmoidal fit of temperature dependent emission intensity integrals was employed. The fit Eq. 3, where *y(x)* is normalized emission integral value at given *x*, the independent variable *x* is the temperature, A_1 is initial value (left horizontal asymptote), A_2 is the final value (right horizontal asymptote), x_0 is the center (point of inflection, $x_0 = TQ_{1/2}$) of the sigmoid, and *dx* is the change in *x* corresponding to the most significant change in *y(x)* values. Fittings were performed on normalized emission intensity integral data; therefore, the A_1 and A_2 values were set to 1 and 0, respectively.[48]

$$y(x) = A_2 + \frac{A_1 - A_2}{1 + e^{(x - x_0)dx}} \quad (3)$$

The obtained results revealed that Sr_2SnO_4:0.5%Eu^{3+} and $Sr_3Sn_2O_7$:0.5%Eu^{3+} phosphors lose half of their efficiency at around 328 and 421 K, respectively. Therefore, $Sr_3Sn_2O_7$ host material is more thermally stable than Sr_2SnO_4. This is in a good agreement with previous work that claimed that mechanoluminescence and photoluminescence intensities are very dependent on the number of perovskite units in an intra-layer and increase in order $Sr_3Sn_2O_7$ > Sr_2SnO_4 > $SrSnO_3$.[16]

The temperature dependent PL lifetime values of Sr_2SnO_4:0.5%Eu^{3+} sample showed a good bi-exponential fit in temperature region from 80 to 340 K (Figure 10a). However, at higher temperature the standard deviation values of τ_1 started to increase rapidly. In the temperature range from 80 to 420 K the curve shows three maximum values peaked at about 200, 300 and 360 K. This lifetime enhancement

process may arise from a local lattice relaxation around the rare-earth ion in the two-dimensional structures. This complex process consists of two independent SnO_6 octahedral rotations around tetragonal $[100]_T$- and $[010]_T$-axes ($\alpha \neq \beta$).[49] The phase transition *Pccn*→*Bmab* at 420 K in Sr_2SnO_4 structure is well consistent with the neutron diffraction studies carried by Fu *et al.*[13] However, the second phase transition *Bmab*→*I4/mmm* may occur at lower temperature of 480–500 K, comparing with Fu *et al.* results at 573 K. Such inaccuracy may be a result of large gap between two measured temperature points (473–573 K). In temperature range 400–480 K there is one maximum corresponding to equal tilts ($\alpha = \beta$). At higher temperature ($T \geq$ 480–500 K), there are no tilts ($\alpha = \beta = 0$) and corresponding space group is *I4/mmm*.

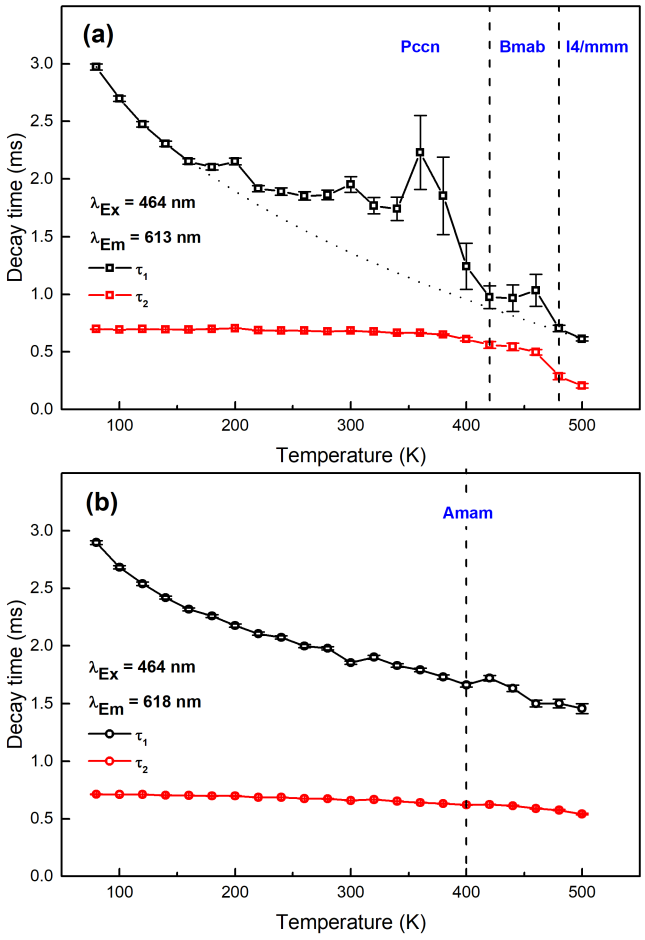

Figure 10. Temperature dependent PL lifetime values of (a) Sr_2SnO_4:0.5%Eu^{3+} and (b) $Sr_3Sn_2O_7$:0.5%Eu^{3+} samples.

In $Sr_3Sn_2O_7$ structure the Eu^{3+} ion response to the changes in coordination environment is weaker than in Sr_2SnO_4 (Figure 10b). In $Sr_3Sn_2O_7$ structure, Sr^{2+}/Eu^{3+} atoms are separated by two perovskite layers rather than one, as in Sr_2SnO_4 host. Moreover, the band gap values are different for both hosts, which affects (governs) the character of luminescence.[50] It is difficult to say about the origin of minimum peaked at 300 K in the temperature dependent emission decay constant in $Sr_3Sn_2O_7$:0.5%Eu^{3+} sample. Most likely, it is due to water molecules intercalated into crystal lattice as was reported elsewhere.[51-52] Upon heating the intercalated solid ice converted to liquid, c-axis decrease with decreasing distortion, which affects the decay time. A weak enhancement of decay time values at 400 K is due to negative thermal expansion, which is in a good agreement with structural and dielectric data presented in this work.

Figure 11 represents the fragments of CIE 1931 chromaticity diagram with color points of $Sr_2SnO_4:Eu^{3+}$ and $Sr_3Sn_2O_7:Eu^{3+}$. With increasing Eu^{3+} concentration, the *x* values show an increasing trend and the *y* values show a decreasing trend. It should also be noted that the color points are located directly on or are very close to the edge of CIE 1931 color space diagram indicating high color saturation.

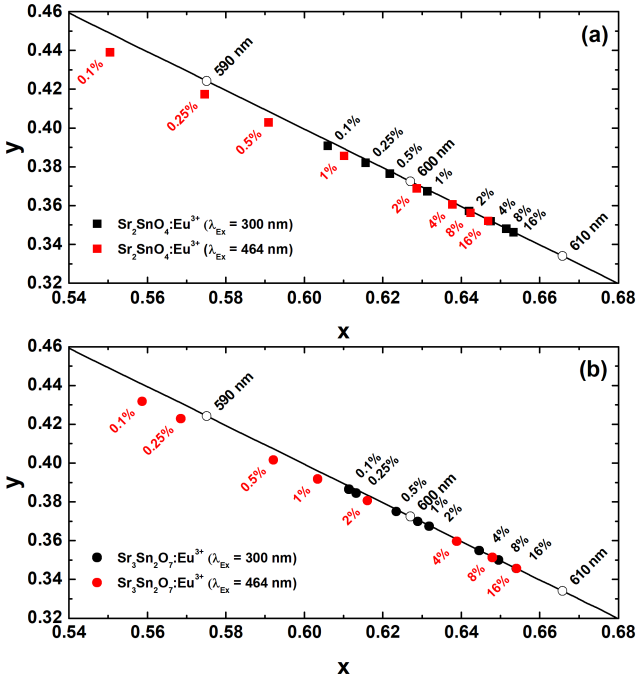

Figure 11. CIE1931 color points of: (a) $Sr_2SnO_4:Eu^{3+}$ and (b) $Sr_3Sn_2O_7:Eu^{3+}$for different Eu^{3+}concentrations.

Conclusions

The Ruddlesden-Popper compound $Sr_3Sn_2O_7$ undoped or doped with 0.5 mol% of Eu^{3+} exhibit a series of temperature-induced structural transformations. In the temperature range of about 390–430 K, two of three lattice parameters decrease indicating a negative thermal expansion along *a*- and *b*-axes, while the structure remains the same (orthorhombic *Amam*) and the unit cell volume increases monotonically. Above about 730 K, $Sr_3Sn_2O_7$ ($Sr_3Sn_2O_7$:0.5%Eu^{3+}) is tetragonal with the *I*4/*mmm* space group and its *c*-parameter decreases with increasing the temperature. The observed temperature behavior of the lattice parameters is reversible with a small hysteresis and upon heating and cooling. Dielectric permittivity of the $Sr_3Sn_2O_7$ ceramics is rather low, and is dominated by electrical conductivity at temperatures above 390 K. The main charge carriers originate from deep defects, which reside close to the Fermi level. A dielectric anomaly observed is associated with a phase transition around 390 K.

The luminescence spectra of Sr_2SnO_4:Eu^{3+} and $Sr_3Sn_2O_7$:Eu^{3+} phosphors are very similar and consistent with low symmetry environment around Eu^{3+} ion. The use of Eu^{3+} as a luminescence probe at cryogenic conditions revealed that lanthanide ions occupy at least 3 and 4 crystallographic sites in Sr_2SnO_4 and $Sr_3Sn_2O_7$, respectively. It was demonstrated, that temperature dependent lifetime measurements are extremely sensitive to variation in coordination environment around Eu^{3+} and can be successfully used for monitoring of phase transitions in these two members of Ruddlesden-Popper compounds. Moreover, the luminescence behavior of other lanthanide ions incorporated as dopants can indicate phase transitions or isostructural transformation in a variety of host structures. We propose that this approach could be both universal and convenient, since it is non-destructive, easy available and doesn't require single crystal or dense ceramic samples. The technique offers a simple tool for gaining insight into the important category of perovskites and perovskite-related compounds.

Acknowledgements. The study was funded from the European Community's social foundation under Grant Agreement No. VP1-3.1-ŠMM-08-K-01-004/KS-120000-1756. The part of this work done in the University of Aveiro was supported by project TUMOCS. This project has received funding from European Union's Horizon 2020 research and innovation program under the Marie Skłodowska-Curie grant agreement No. 645660. Additional support was provided by the Flexible Integrated Energy Systems

(FLEXIS) research operation funded by the Welsh European Funding Office (WEFO) through the Welsh Government.

ASSOCIATED CONTENT

The Supporting Information is available free of charge on the ACS Publications website at DOI: XXXXXXX. XRD data, TG-DSC curves of precursor gel, SEM images of powder and pellet samples, concentration quenching data, emission decay curves, temperature dependent mono-exponential emission decay values, asymmetric ratio versus temperature data, magnified $^5D_0 \rightarrow {}^7F_0$ and $^5D_0 \rightarrow {}^7F_1$ transitions of Eu^{3+} ion in Sr_2SnO_4 and $Sr_3Sn_2O_7$ host materials and unit cell of both hosts together with polyhedral structure around coordinating ions.

AUTHOR INFORMATION

Corresponding Author

*E-mail: (A.S.) *Andrius.stanulis@swansea.ac.uk*; (A.R.B.) a.r.barron@swansea.ac.uk

ORCHID

Andrew R. Barron: 0000-0002-2018-8288

Notes

The authors declare no competing financial interest.

References

1. Goodenough, J. B., Electronic and ionic transport properties and other physical aspects of perovskites. *Rep. Prog. Phys.* **2004,** *67*, 1915-1993.

2. Benedek, N. A.; Rondinelli, J. M.; Djani, H.; Ghosez, P.; Lightfoot, P., Understanding ferroelectricity in layered perovskites: new ideas and insights from theory and experiments. *Dalton Trans.* **2015**, 10543-10558.

3. Mulder, A. T.; Benedek, N. A.; Rondinelli, J. M.; Fennie, C. J., Turning ABO_3 antiferroelectrics into ferroelectrics: Design rules for practical rotation-driven ferroelectricity in double perovskites and $A_3B_2O_7$ Ruddlesden-Popper compounds. *Adv. Funct. Mater.* **2013,** *23*, 4810-4820.

4. Benedek, N. A., Origin of ferroelectricity in a family of polar oxides: The Dion—Jacobson phases. *Inorg. Chem.* **2014,** *53*, 3769-3777.

5. Ruddlesden, S. N.; Popper, P., New compounds of the K_2NiF_4 type. *Acta Cryst.* **1957,** *10* (8), 538-539.

6. Ruddlesden, S. N.; Popper, P., The compound $Sr_3Ti_2O_7$ and its structure. *Acta Cryst.* **1958,** *11*, 54-55.

7. Benedek, N. A.; Fennie, C. J., Hybrid improper ferroelectricity: A mechanism for controllable polarization-magnetization coupling. *Phys. Rev. Lett.* **2011,** *106*, 107204.

8. Oh, Y. S.; Luo, X.; Huang, F.-T.; Wang, Y.; Cheong, S.-W., Experimental demonstration of hybrid improper ferroelectricity and the presence of abundant charged walls in $(Ca,Sr)_3Ti_2O_7$ crystals. *Nat. Mater.* **2015,** *14*, 407-413.

9. Wang, Y.; Huang, F. T.; Luo, X.; Gao, B.; Cheong, S. W., The first room-temperature ferroelectric Sn insulator and its polarization switching kinetics. *Adv. Mater.* **2017,** *29*, 1601288.

10. Green, M. A.; Prassides, K.; Day, P.; Stalick, J. K., Structural properties of A_2SnO_4 (A = Ba, Sr). A neutron diffraction study. *J. Chem. Soc. Faraday Trans.* **1996,** *92*, 2155-2159.

11. Green, M. A.; Prassides, K.; Day, P.; Neumann, D. A., Structure of the n=2 and n=∞ member of the Ruddlesden-Popper series, $Sr_{n+1}Sn_nO_{3n+1}$. *Int. J. Inorg. Mater.* **2000,** *2*, 35-41.

12. Fu, W. T.; Visser, D.; IJdo, D. J. W., High-resolution neutron powder diffraction study on the structure of Sr_2SnO_4. *J. Solid State Chem.* **2002,** *169*, 208-213.

13. Fu, W. T.; Visser, D.; Knight, K. S.; Ijdo, D. J. W., Neutron powder diffraction study of phase transitions in Sr_2SnO_4. *J. Solid State Chem.* **2004,** *177*, 4081-4086.

14. Lei, B.; Man, S.-Q.; Liu, Y.; Yue, S., Luminescence properties of Sm^{3+}-doped $Sr_3Sn_2O_7$ phosphor. *Mater. Chem. Phys.* **2010,** *124*, 912-915.

15. Kamimura, S.; Yamada, H.; Xu, C.-N., Strong light emission from stress-activated perovskite-related oxides. *Mater. Res. Soc. Symp. Proc.* **2013,** *1492*, 117-122.

16. Kamimura, S.; Yamada, H.; Xu, C.-N., Strong reddish-orange light emission from stress-activated $Sr_{n+1}Sn_nO_{3n+1}:Sm^{3+}$ ($n = 1, 2, \infty$) with perovskite-related structures. *Appl. Phys. Lett.* **2012,** *101*, 091113.

17. Wang, C.; Jin, Y.; Lv, Y.; Ju, G.; Chen, L.; Li, Z.; Hu, Y., A bifunctional phosphor $Sr_3Sn_2O_7:Eu^{3+}$: Red luminescence and photochromism properties. *J. Lumin.* **2017,** *192*, 337-342.

18. Liu, R. S., *Phosphors, up conversion nano particles, quantum dots and their applications*. Springer Singapore: 2016.

19. Buenzli, J. C. G.; Plancherel, D.; Pradervand, G. O., The europium(III) ion as luminescent probe: structural investigation of complexes between europium nitrate and two polyethers. *J. Phys. Chem.* **1989,** *93*, 980-984.

20. Gupta, S. K.; Bhide, M. K.; Godbole, S. V.; Natarajan, V., Probing site symmetry around Eu^{3+} in nanocrystalline ThO_2 using time resolved emission spectroscopy. *J. Am. Ceram. Soc.* **2014,** *97*, 3694-3701.

21. Stanulis, A.; Katelnikovas, A.; Van Bael, M.; Hardy, A.; Kareiva, A.; Justel, T., Photoluminescence of Pr^{3+}-doped calcium and strontium stannates. *J. Lumin.* **2016,** *172*, 323-330.

22. Townsend, P. D.; Yang, B.; Wang, Y., Luminescence detection of phase transitions, local environment and nanoparticle inclusions. *Contemp. Phys.* **2008,** *49*, 255-280.

23. Stanulis, A.; Sakirzanovas, S.; Van Bael, M.; Kareiva, A., Sol–gel (combustion) synthesis and characterization of different alkaline earth metal (Ca, Sr, Ba) stannates. *J. Sol-Gel Sci. Techn.* **2012,** *64*, 643-652.

24. Rodríguez-Carvajal, J., Recent advances in magnetic structure determination by neutron powder diffraction. *Physica B* **1993,** *192*, 55-69.

25. Titov, Y. A.; Slobodyanyk, M. S.; Krayevska, Y. A., Peculiarities of formation and isomorphism of Ruddlesden-Popper compounds $Sr_{n+1}B_nO_{3n+1}$-type (B = Sn, Ti, n = 1, 2). *Ukr. Khim. Zh. (Russ. Ed.)* **2008,** *74*, 7-17.

26. Yoshida, S.; Akamatsu, H.; Tsuji, R.; Hernandez, O.; Padmanabhan, H.; Sen Gupta, A.; Gibbs, A. S.; Mibu, K.; Murai, S.; Rondinelli, J. M.; Gopalan, V.; Tanaka, K.; Fujita, K., Hybrid improper ferroelectricity in $(Sr,Ca)_3Sn_2O_7$ and beyond: universal relationship between ferroelectric transition temperature and tolerance factor in n = 2 Ruddlesden–Popper phases. *J. Am. Chem. Soc.* **2018,** *140*, 15690-15700.

27. Senn, M. S.; Bombardi, A.; Murray, C. A.; Vecchini, C.; Scherillo, A.; Luo, X.; Cheong, S. W., Negative thermal expansion in hybrid improper ferroelectric Ruddlesden-Popper perovskites by symmetry trapping. *Phys. Rev. Lett.* **2015,** *114*, 035701.

28. Gibbs, A. S.; Knight, K. S.; Lightfoot, P., High-temperature phase transitions of hexagonal $YMnO_3$. *Phys. Rev. B* **2011,** *83*, 094111.

29. Salak., A. N.; Prokhnenko, O.; Ferreira, V. M., Temperature evolution of the crystal structures in $La(Mg_{1/2}Ti_{1/2})O_3$ perovskite: Relation to the microwave dielectric properties. *J. Phys. Condens. Mat.* **2008,** *20*, 085210.

30. Kamimura, S.; Obukuro, Y.; Matsushima, S.; Nakamura, H.; Arai, M.; Xu, C.-N., First-principles energy band calculation of Ruddlesden–Popper compound $Sr_3Sn_2O_7$ using modified Becke–Johnson exchange potential. *J. Solid State Chem.* **2015,** *232*, 163-168.

31. Cohen, R. E.; Krakauer, H., Lattice dynamics and origin of ferroelectricity in $BaTiO_3$: Linearized-augmented-plane-wave total-energy calculations. *Phys. Rev. B* **1990,** *42* (10), 6416-6423.

32. Waghmare, U. V.; Rabe, K. M., Ab initio statistical mechanics of the ferroelectric phase transition in $PbTiO_3$. *Phys. Rev. B* **1997,** *55*, 6161-6173.

33. Jaffe, B.; Cook, W. R.; Jaffe, H. L., *Piezoelectric ceramics*. Academic Press: London; New York, 1971.

34. Chen, Y. C.; Chang, Y. H.; Tsai, B. S., Influence of processing conditions on synthesis and photoluminescence of Eu^{3+} activated strontium stannate phosphors. *J. Alloy. Compd.* **2005,** *398*, 256-260.

35. Y. Chen, X.; Liu, G., The standard and anomalous crystal-field spectra of Eu^{3+}. *J. Solid State Chem.* **2005,** *178*, 419-428.

36. Zhou, J.; Xie, L.; Zhong, J.; Liang, H.; Zhang, J.; Wu, M., Site occupancy and luminescence properties of Eu^{3+} in double salt silicate $Na_3LuSi_3O_9$. *Opt. Mater. Express* **2018,** *8* (4), 736-743.

37. K. Gupta, S.; Sahu, M.; Krishnan, K.; K. Saxena, M.; Natarajan, V.; V. Godbole, S., Bluish white emitting Sr_2CeO_4 and red emitting Sr_2CeO_4:Eu^{3+} nanoparticles: Optimization of synthesis parameters, characterization, energy transfer and photoluminescence. *J. Mater. Chem. C* **2013,** *1*.

38. Shionoya, S.; Yen, W. M.; Phosphor research, s., *Phosphor handbook*. CRC Press: Boca Raton; Boston; London, 1999.

39. Shannon, R., Revised effective ionic radii and systematic studies of interatomic distances in halides and chalcogenides. *Acta Cryst. A* **1976,** *32*, 751-767.

40. Wang, D.; Chang, W.; Ma, B.; Wang, Y., Unusual concentration quenching of Sm^{3+} and Eu^{3+} doped Sr_2SnO_4 under UV and NUV excitation. *J. Solid State Chem.* **2017,** *253*, 382-388.

41. Holz, R. C.; Thompson, L. C., Spectroscopic and structural characterization of the nine-coordinate adduct of tris(dipivaloylmethanato)europium(III) with 2,2':6',2"-terpyridine. *Inorg. Chem.* **1988,** *27*, 4640-4644.

42. Gerkin, R. E.; Reppart, W. J., Structures of holmium bromate enneahydrate at 168 and 294 K and their implications for the isomorphic series of rare-earth bromate enneahydrates. *Acta Cryst. C* **1987,** *43*, 623-631.

43. Helmholz, L., The crystal structure of neodymium bromate enneahydrate, $Nd(BrO_3)_3 \cdot 9H_2O$. *J. Am. Chem. Soc.* **1939,** *61*, 1544-1550.

44. Moret, E.; Nicolo, F.; Bünzli, J.-C. G.; Chapuis, G., Structural and luminescence study of europium and terbium tris(bromate) nonahydrates. *J. Less Common Met.* **1991,** *171*, 273-300.

45. Bünzli, J. C. G.; Pradervand, G. O., The Eu(III) ion as luminescent probe: Laser-spectroscopic investigation of the metal ion sites in an 18-crown-6 complex. *J. Chem. Phys.* **1986,** *85*, 2489-2497.

46. Choppin, G. R.; Bünzli, J. C. G., *Lanthanide probes in life, chemical, and earth sciences: theory and practice*. Elsevier: Amsterdam ; New York, 1989; p xiii, 432 p.

47. Binnemans, K., Interpretation of europium(III) spectra. *Coordin. Chem. Rev.* **2015,** *295*, 1-45.

48. Katelnikovas, A.; Plewa, J.; Sakirzanovas, S.; Dutczak, D.; Enseling, D.; Baur, F.; Winkler, H.; Kareiva, A.; Justel, T., Synthesis and optical properties of $Li_3Ba_2La_3(MoO_4)_8:Eu^{3+}$ powders and ceramics for pcLEDs. *J. Mater. Chem.* **2012,** *22*, 22126-22134.

49. Kamimura, S.; Xu, C.-N.; Yamada, H.; Marriott, G.; Hyodo, K.; Ohno, T., Near-infrared luminescence from double-perovskite $Sr_3Sn_2O_7:Nd^{3+}$: A new class of probe for in vivo imaging in the second optical window of biological tissue. *J. Ceram. Soc. Jpn.* **2017,** *125*, 591-595.

50. Dorenbos, P., The Eu^{3+} charge transfer energy and the relation with the band gap of compounds. *J. Lumin.* **2005,** *111*, 89-104.

51. Lehtimäki, M.; Yamauchi, H.; Karppinen, M., Stability of Ruddlesden–Popper-structured oxides in humid conditions. *J. Solid State Chem.* **2013,** *204*, 95-101.

52. Liu, S.; Avdeev, M.; Liu, Y.; Johnson, M. R.; Ling, C. D., A new n = 4 layered Ruddlesden–Popper phase $K_{2.5}Bi_{2.5}Ti_4O_{13}$ showing stoichiometric hydration. *Inorg. Chem.* **2016,** *55*, 1403-1411.

For Table of Contents Only

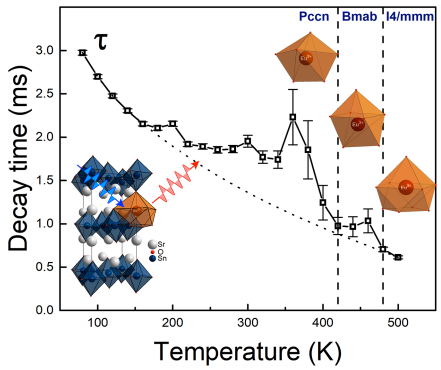

Temperature dependent lifetime measurements can be successfully applied to monitor phase transitions in perovskites and perovskite-related compounds.